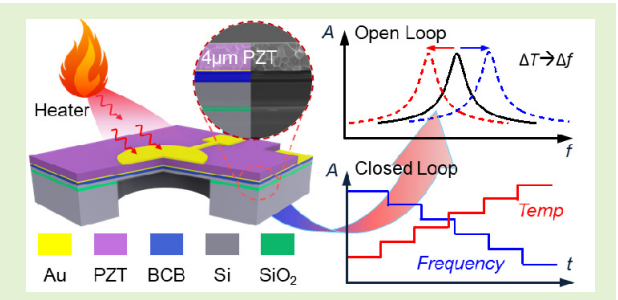
IEEE SENSORS JOURNAL, VOL. XX, NO. XX, MONTH X, XXXX

Micromachined Thin Film Ceramic PZT Multimode Resonant Temperature Sensor

Wen Sui, *Graduate Student Member, IEEE*, Tahmid Kaisar, *Graduate Student Member, IEEE*, Haoran Wang, Yihao Wu, Jaesung Lee, *Member, IEEE*, Huikai Xie, *Fellow, IEEE*, and Philip X.-L. Feng, *Senior Member, IEEE*

Abstract—Micromachined thin-film lead zirconate titanate (PZT) retains exceptional piezoelectric and energy-harvesting capabilities, thus offering an excellent platform for enabling efficient piezoelectric microsystems on chip. Here, we design fabricate thin-film ceramic PZT piezoelectric systems microelectromechanical (MEMS) operating flexural-mode resonances, by using wafer bonding and chemical mechanical polishing (CMP) techniques. We describe the experimental demonstration of an integrated multimode resonant PZT MEMS temperature sensor. The three resonance modes examined (at 1.1, 3.6, 6.8MHz) all exhibit excellent



linearity and responsivity to temperature variations in the range of 25°C to 211°C, with temperature coefficients of resonance frequency (TCf) at -200ppm/°C to -270ppm/°C for open-loop measurement. We have demonstrated dual-mode temperature sensing with real-time tracking of the resonance frequency using a phase-locked loop (PLL). We have also built a self-sustaining MEMS oscillator and studied the closed-loop TCf. We compare the open-loop and closed-loop TCfs in both air and vacuum and find that the TCf can be affected by heating method, pressure, and measurement scheme. The results extend the understanding of temperature effects on the resonance frequency of PZT MEMS, demonstrate real-time temperature sensing, and pave the way for enabling multifunctional PZT microsystems on chip.

Index Terms—Microelectromechanical systems (MEMS), ceramic PZT, temperature sensor, oscillator, phase-locked loop

I. INTRODUCTION

TOWARDS emerging industry 4.0 with prevailing internet of things (IoT) and the swarm of trillion sensors perspective, new advances in miniaturized, ultralow-power or self-powering, multifunctional integrated sensors are increasingly demanded [1],[2]. Miniature temperature sensors,

This work was supported by the National Institutes of Health (NIH) under Award R01EB020601, National Science Foundation (NSF) ECCS EAGER Program (Grant #2221881), and the Finish Line Award from Graduate School, University of Florida. (Wen Sui and Tahmid Kaisar contributed equally to this work.)

Wen Sui, Tahmid Kaisar, Yihao Wu and Philip X.-L. Feng are with the Department of Electrical and Computer Engineering, Herbert Wertheim College of Engineering, University of Florida, Gainesville, FL 32611 USA (e-mail: wen.sui@ufl.edu; kaisart@ufl.edu; philip.feng@ufl.edu).

Haoran Wang was with the Department of Electrical and Computer Engineering, Herbert Wertheim College of Engineering, University of Florida, Gainesville, FL 32611. He is now a senior scientist at Applied Materials Inc., Sunnyvale, CA 94086, USA.

Jaesung Lee was with the Department of Electrical and Computer Engineering, Herbert Wertheim College of Engineering, University of Florida, Gainesville, FL 32611. He is now an Assistant Professor with the Department of Electrical and Computer Engineering, College of Engineering, The University of Texas at El Paso, El Paso, TX 79968 USA.

Huikai Xie was with the Department of Electrical and Computer Engineering, Herbert Wertheim College of Engineering, University of Florida, Gainesville, FL 32611. He is now with School of Integrated Circuits and Electronics, Beijing Institute of Technology (BIT), Beijing 100081, China.

in particular, while being ubiquitous and having various existing solutions in conventional methods (e.g., thermistors, diodes, transistors, etc.), still face new challenges in emerging applications, such as in smart buildings and industry plants, self-driving vehicles (e.g., monitoring the temperature of engine or other critical parts), fire-fighting drones, and medical implants, etc. [3],[4]. High precision, energy efficiency, and harsh-environment resilience are essential in such scenarios while conventional thermistor/diode options are increasingly insufficient or unfit. Harsh environments are not only limited to space and areas affected by natural hazards [5],[6]. There are also various industrial applications which impose harsh conditions on devices. Jet engines or downhole gas and oil industry, for instance, subject monitoring devices to high temperatures and pressures [7]. There is a high demand for passive wireless temperature sensing in various applications, especially inaccessible locations, and hazardous environments where long lifetime is essential, or harsh environments where battery lifetime can be severely shortened [8].

Resonant sensors have frequency as output and have become a powerful solution to sensing many physical parameters such as mass, pressure, temperature, and viscosity. Remote temperature sensors were demonstrated in 1987 based on lithium niobate (LiNbO₃) surface acoustic wave (SAW) resonators [9]. A plethora of devices have recently been developed and are currently in widespread use [10]. Resonant

XXXX-XXXX © XXXX IEEE. Personal use is permitted, but republication/redistribution requires IEEE permission. See http://www.ieee.org/publications_standards/publications/rights/index.html for more information.

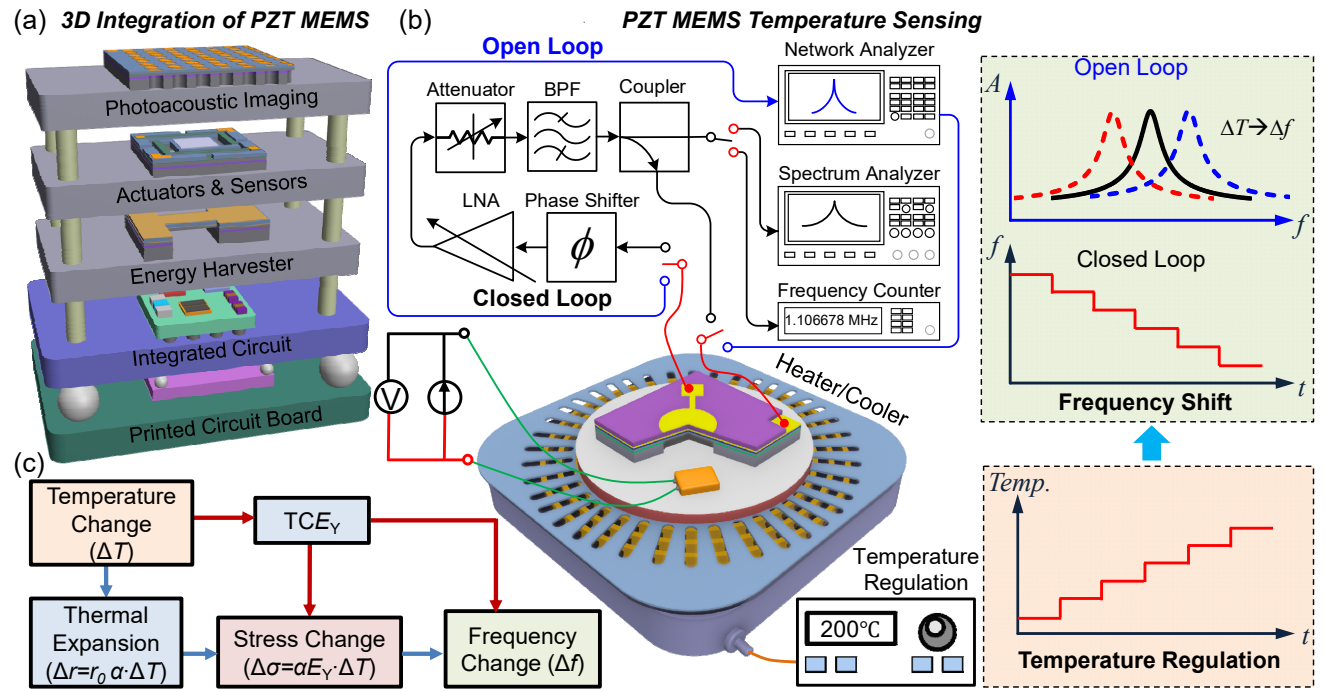


Fig. 1. Scientific background and experimental design. (a) A vision of future 3D integration of PZT MEMS with integrated circuits (ICs). (b) Illustration of the device platform and measurement scheme for both open loop and closed loop, where BPF represents band pass filter and LNA represents low-noise amplifier. (c) Block diagram shows effects of varying temperature on the resonance frequency. TCE_Y represents the temperature coefficient of Young's modulus, α is the thermal expansion coefficient, r_0 represents the initial radius.

temperature sensors have often been fabricated using piezoelectric crystals, such as LiNbO₃ or quartz. The high responsivity to temperature in particular cuts of quartz crystals has made it possible to manufacture sensors with very high resolution (0.001°C) [11]. Despite this feature, the main disadvantages of these sensors are their relatively large sizes and the incompatibility of their fabrication processes with microfabrication mainstream silicon and scalable manufacturing technologies [12]. Microelectromechanical systems (MEMS) technology has witnessed tremendous development over recent decades. MEMS devices are sensitive to external perturbations, making them excellent candidates for physical sensors, particularly resonant-mode sensors for physical stimuli and perturbations, such as pressure, vibration, humidity, mass, temperature, etc. [13],[14],[15].

Regarding MEMS resonators for temperature sensing applications, it is essential to investigate the temperature effects on the resonance frequency, and a large absolute value of the temperature coefficient of resonance frequency (TCf) is preferred. To date, TCf values (TCfs hereafter for simplicity) of MEMS with diverse structures based on various materials (Si, AlN, GaN, SiC, etc.) have been extensively reported [16], [17], [18], [19], [20]. However, the majority of research has concentrated on achieving near-zero TCf through improving structural design, doping, and stress regulation, so as to enable MEMS for timing references [21], [22], [23], [24], [25]. Most TCfs reported in literatures are less than 100ppm/°C. Only few studies are dedicated to obtaining large TCfs, which are required for temperature sensing applications [26], [27]. On the other hand, three-dimensional (3D) integration and packaging of MEMS with integrated circuits (ICs) is an emerging technology that could lead to a new paradigm of future highly integrated microsystems, enabling multi-functionality, high performance, small size and low weight, and at low cost [28]. It would be interesting if we had MEMS energy harvesting, MEMS temperature sensor, and integrated circuits (ICs) all on one silicon die.

Micromachined thin-film lead zirconate titanate (PZT) retains exceptional piezoelectric and energy-harvesting capabilities, which is an excellent platform for enabling efficient piezoelectric microsystems on chip [29], [30], [31]. PZT piezoelectric micromachined ultrasonic transducers (pMUT) is a versatile technology for ultrasonic sensing and photoacoustic imaging [32], [33]. It would be appealing to have a PZT MEMS temperature sensor which can be self-powered and integrated into PZT pMUT arrays for continuous monitoring and sensing in ordinary and harsh environments. A vision of future 3D integration of PZT MEMS with ICs is illustrated in Fig. 1a. In terms of fabrication, sputtered PZT or sol-gel PZT films are commonly limited by high processing temperature, high stress, low deposition rate and small thickness [34], [35]. Ceramic PZT materials with a wide range of thickness, on the other hand, can effectively boost the piezoelectric response and reduce the processing temperature [36], [37]. However, its fragileness makes it challenging to thin the ceramic PZT down to sub-10µm thickness.

In this work, we design and fabricate thin-film ceramic PZT piezoelectric MEMS transducers operating on flexural-mode resonances by using wafer bonding and chemical mechanical polishing (CMP) techniques. We thoroughly investigate the effect of temperature on the resonance of PZT MEMS under different conditions using various heating techniques, pressures, and measurement approaches. We have demonstrated temperature sensing with real-time tracking of the resonance frequency using a phase-locked loop (PLL) and by building a self-sustaining MEMS oscillator.

II. DESIGN OF EXPERIMENT

A. Structural Design of PZT MEMS

The multimode resonance frequency of a circular diaphragm resonator can be expressed as [38]

$$f_n = \left(\frac{k_n r}{2\pi}\right) \sqrt{\frac{D}{\rho t r^4} \left[(k_n r)^2 + \frac{\gamma r^2}{D} \right]},\tag{1}$$

where *n* represents the mode number, *r* is the radius, $(k_n r)^2$ is a numerically calculated modal parameter $((k_0r)^2=10.215,$ $(k_1r)^2=21.260$, $(k_2r)^2=34.877$, $(k_3r)^2=39.771$)), ρ denotes the volume mass density, t is the thickness, γ refers to the built-in tension (in $\lceil N/m \rceil$, or stress $\lceil N/m^2 \rceil$ or Pa times thickness), and D is the flexural rigidity, $D=E_Yt^3/[12(1-v^2)]$ in which E_Y and v are Young's modulus and Poisson's ratio, respectively. Equation (1) yields a mixed elasticity model, in which both flexural rigidity (dominated by the thickness and elastic modulus) and built-in tension (stress) play key roles in determining the resonance frequency. As $\gamma r^2/D$ goes very small and negligible in (1), flexural rigidity D dominates the frequency, and the model approaches the plate limit.

$$f_n = \frac{(k_n r)^2}{2\pi r^2} \sqrt{\frac{D}{\rho t}},\tag{2}$$

For a circulate plate with multilayers, as illustrated in Fig. 2, the effective flexural rigidity and mass density can be expressed

$$D = \sum_{i} \left(\frac{E_{Yi}}{1 - v_i^2} \right) \left(\frac{t_i^3}{12} + d_i^2 t_i \right),$$

$$\rho = \sum_{i} \left(\rho_i \frac{t_i}{t} \right).$$
(4)

$$\rho = \sum_{i} \left(\rho_i \frac{t_i}{t} \right). \tag{4}$$

Here E_{Yi} , v_i , t_i , and ρ_i are Young's modulus, Poisson's ratio, thickness, and volume mass density of the ith layer, respectively, and d_i is the distance between the mid-plane of the ith layer to the neutral plane. By controlling the thickness of each layer, the neutral plane is set within benzo-cyclo-butene (BCB) layer (Fig. 2), as indicated by

$$Z_n = \frac{\sum_{l=1}^{m} \frac{E_{Y_l} Z_l t_l}{1 - \nu_l^2}}{\sum_{l=1}^{m} \frac{E_{Y_l} t_l}{1 - \nu_l^2}},$$
 (5)

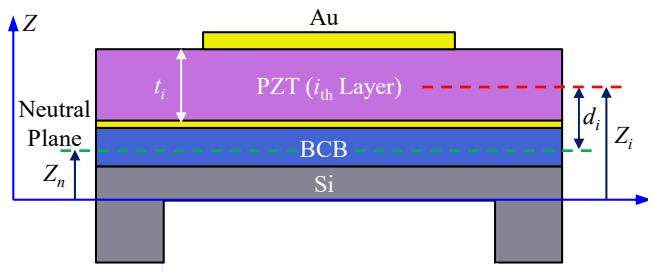


Fig. 2. Schematic diagram of the cross-sectional view of the designed

where Z_n defines the distance from the neutral plane to the reference plane and Z_i is the distance from the reference plane to the mid plane of the i_{th} layer. Table I summarizes the key properties of each structure layer. We first estimated the diameter of the device with (2) to obtain a device with the target frequency at 1.1MHz. We then performed finite element method (FEM) simulation to guide the structure design. Starting from the calculated values, multiple iterations are performed in COMSOL Multiphysics to accurately find the corresponding device dimensions for the target frequencies. It has been found that the diaphragm with the diameter of 244µm yields the fundamental-mode resonant frequencies of 1.1MHz. The diameter of the top electrode is 172µm, which is designed with a 70% diameter coverage of the diaphragms for optimal transduction.

TABLE I STRUCTURAL AND MATERIAL PROPERTIES

Structure	Material	Thickness [μm]	Young's Modulus [GPa]	Mass Density [kg/m³]	Poisson's Ratio
Supporting Layer	Si	3	170	2329	0.28
Bonding Layer	BCB	2	2.9	990	0.34
Bottom Electrode	Au	0.1	70	19300	0.44
Piezoelectric Layer	PZT	4	64	7870	0.31
Top Electrode	Au	0.35	70	19300	0.44

B. Measurement Scheme

A customized heating and temperature sensing stage is

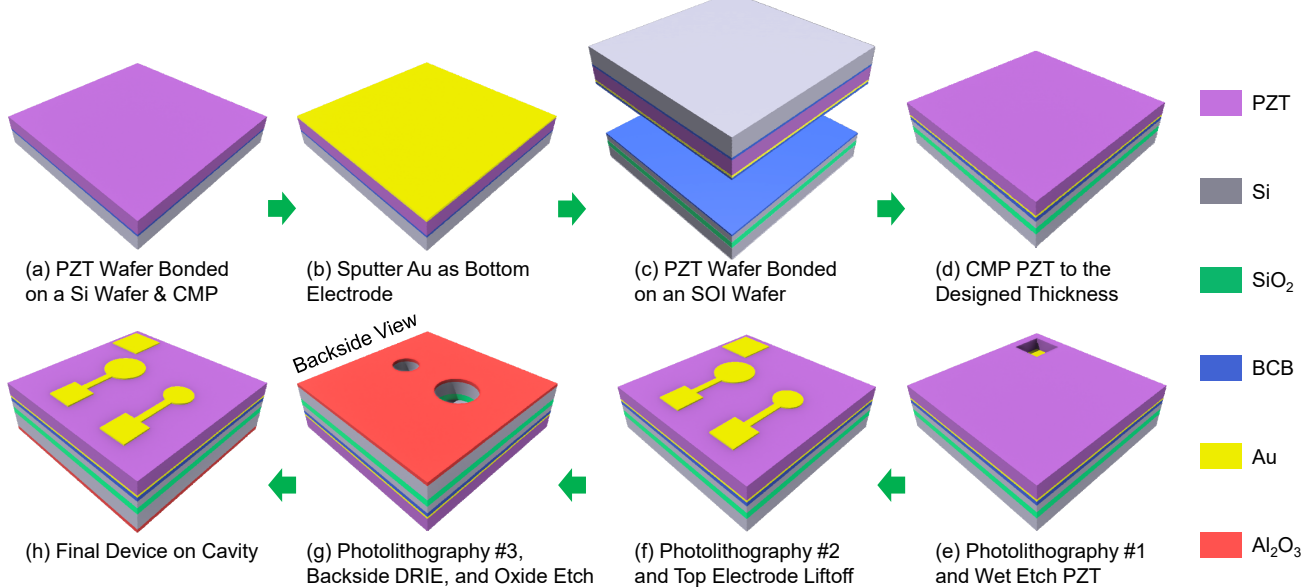


Fig. 3. Fabrication process flow of the PZT MEMS in this work. (a) Bond PZT wafer on a Si wafer and CMP. (b) Sputter Au. (c) Bond PZT wafer on an SOI wafer. (d) CMP PZT. (e) Wet etch PZT. (f) Define top Au electrode. (g) Backside etch Si and SiO2. (h) Final device on cavity.

utilized to precisely regulate the device's temperature, as shown in Fig. 1b. We apply a resistive temperature sensor to the surface of either a metal ceramic heater element (25°C to 211°C) or a Peltier stage (0°C to ~125°C) utilizing nickel paste, to provide real-time monitoring of the heater's temperature. The MEMS die is then wired-bonded within a ceramic package, placed adjacent to the temperature sensor, and seated atop the heater. The highest temperature is well below the Curie temperature (242°C) of PZT. Open-loop multimode resonances are measured by a network analyzer. Real-time tracking of the resonance frequency with temperature changing is achieved by either building a self-sustaining MEMS oscillator or a PLL. Fig. 1c shows the block diagram of temperature effects on the resonance frequency.

III. FABRICATION OF PZT MEMS

The key fabrication processes of the PZT MEMS devices include temporary bonding of a ceramic PZT wafer to a Si wafer, CMP of ceramic PZT, and permanent bonding of PZT thin film with an SOI wafer [39]. Fig. 3 shows the detailed fabrication process flow. Firstly, the 500 µm-thick ceramic PZT wafer was bonded with a Si wafer using BCB, and thinned down to 100µm with a smooth surface by CMP, followed by sputtering of 100nm Au as the bottom electrode. After that, the PZT wafer was permanently bonded with an SOI wafer by BCB at 200°C. Next, the PZT wafer was further thinned down to the designed thickness of 4µm by carefully removing the Si, BCB, and PZT in sequence. The thin ceramic PZT was then patterned to expose the bottom electrode by wet etching with diluted fluoroboric acid (HBF₄) [40]. Next, the top electrode pattern was defined by photolithography and formed by Au sputtering and liftoff process. Finally, the cavities were defined by a

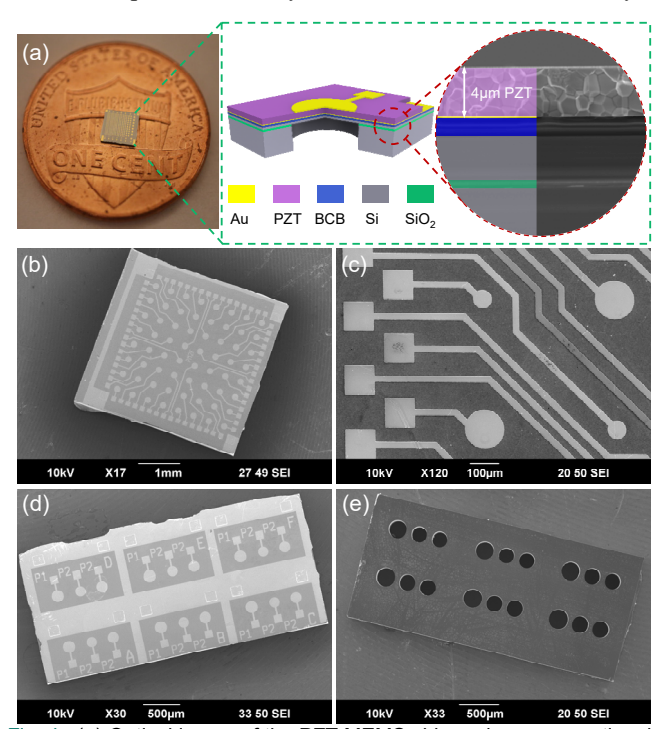


Fig. 4. (a) Optical image of the PZT MEMS chip and a cross sectional view SEM of the multilayers. SEM images of (b) a 8 × 8 PZT MEMS transducer array and (c) the zoom-in view of the top electrodes. SEM images of another chip with single elements in the (d) front and (e) backside view, respectively.

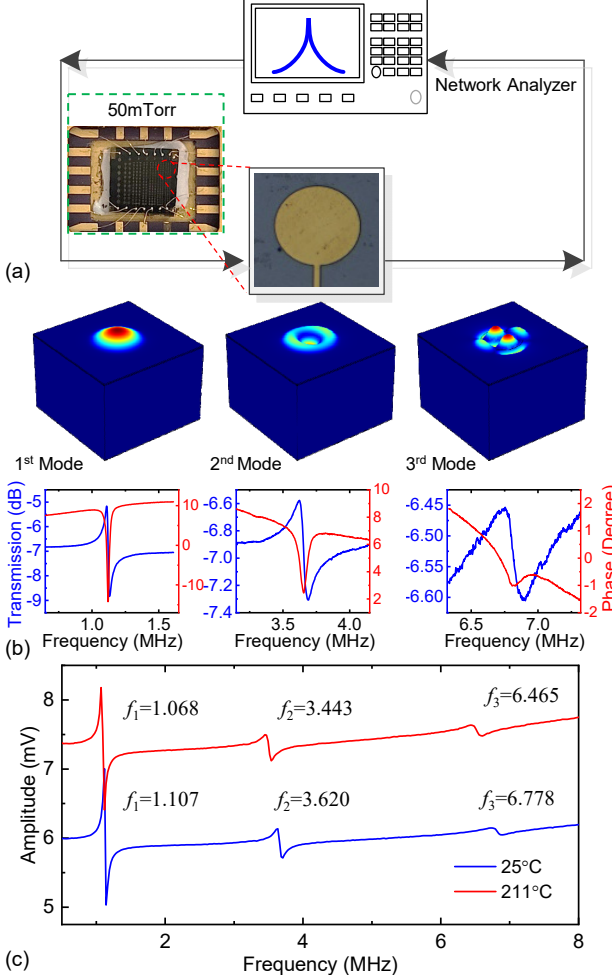


Fig. 5. (a) Scheme of open-loop measurement, with a photo of PZT MEMS die wire-bonded in a ceramic package and a zoomed-in view of a single device with a diameter of 244μm. (b) Multimode resonance measured at room temperature (25°C) and the corresponding mode shapes simulated in COMSOL. (c) Resonance spectra measured in the range from 0.5MHz to 8MHz at 25°C and 211°C, respectively.

photolithography and a backside deep reactive ion etching (DRIE) with an aluminum oxide (Al_2O_3) layer as the hard mask. The Al_2O_3 is patterned and wet etched by diluted hydrofluoric acid (HF).

Various devices with different chip sizes and number of elements have been fabricated. Fig. 4a shows an optical image of a fabricated PZT MEMS chip with the size of 3.5mm $\times 3.5$ mm. The inset shows the device structure and a cross-sectional view scanning electron microscopy (SEM) image, where the thickness of the ceramic PZT layer is measured to be around 4µm. Fig. 4b shows an SEM image of a fabricated 8 \times 8 PZT MEMS transducer array, whose top electrodes are shown in a zoom-in SEM image in Fig. 4c. Fig. 4d and 4e show SEM images of another fabricated chip with single elements in the front and backside views, respectively.

IV. RESULTS AND DISCUSSIONS

A. Temperature-Dependent Multimode Resonances

We first characterize the multimode resonances of circular diaphragm PZT MEMS resonators with diameter of 244µm, at 25°C, by using a network analyzer (Fig. 5a). Three resonance

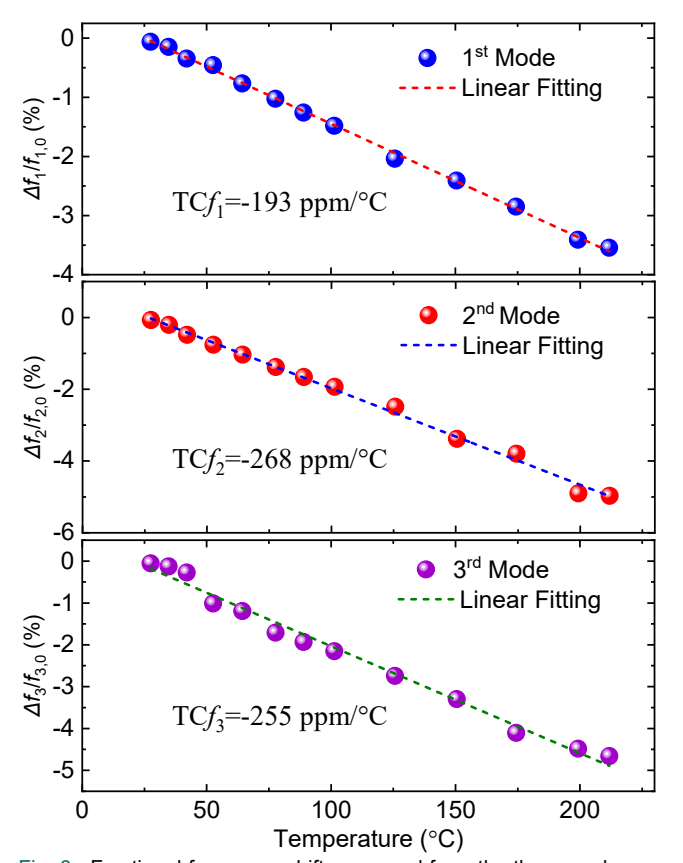


Fig. 6. Fractional frequency shift measured from the three modes vs. varying temperature from 25°C to 211°C, with TCf extraction. modes are observed in the range of 1MHz to 8MHz, f_1 =1.107MHz, f_2 =3.620MHz, f_3 =6.778MHz. For fundamental mode, the device has a O factor of 50 both in air and in vacuum with pressure of 50mTorr. The FEM simulated resonance frequencies match the measurement well, with $f_{S1} = 1.109$ MHz, $f_{S2}=3.698$ MHz, $f_{S3}=6.794$ MHz, and the corresponding mode shapes are shown in Fig. 5b.

To determine the temperature coefficient of resonance frequency, we measure these modes in the temperature range of 25°C to 211°C. The MEMS device chip is mounted in a ceramic package and faced the heater. The resonance frequencies of the three modes are recorded. Fig. 5c shows the resonance spectrum of the PZT MEMS at 25°C and 211°C, respectively.

$$TCf = \frac{1}{f} \frac{\Delta f}{\Delta T},\tag{6}$$

TCf values are evaluated by using $TCf = \frac{1}{f} \frac{\Delta f}{\Delta T}, \tag{6}$ where T is temperature. We find that the resonance frequencies decrease monotonically with increasing temperature (Fig. 6). We plot the frequency shift at different temperatures with respect to its resonance frequency at 25°C for each of the 3 modes, in which a linear relation between $\Delta f/f$ and T is observed from each mode. We then extract an average $TCf_1 = -193$ ppm/°C for the first mode, $TCf_2 = -268ppm/°C$ for the second mode, and $TCf_3 = -255 \text{ ppm/}^{\circ}\text{C}$ for the third mode. The linear temperature dependence and TCf values of the PZT MEMS resonator can be directly exploited for on-chip temperature

Staring from (2), the TCf of a circular diaphragm operating in the plate regimes can be approximately expressed as $TCf \approx \frac{3}{2}\alpha + \frac{TCE_Y}{2}$,

$$TCf \approx \frac{3}{2}\alpha + \frac{TCE_Y}{2},\tag{7}$$

where α is the thermal expansion coefficient, and TCE_Y is the temperature coefficient of Young's modulus. Thus, the monotonic decrease of resonance frequencies is determined by synergistic effects of thermal expansion temperature-dependent Young's modulus. In our case, we should consider the effective thermal expansion coefficient (α $_{\text{eff}}$) and effective TCE_Y of the multilayer structure, which makes it more complicated. As reported, the thermal expansion coefficient of Si and Au changes only slightly over a wide temperature range [41], [42], indicating that they do not play a major role in determining the TCf. On the other hand, the Young's modulus of these materials decreases more noticeably with increasing temperature [43], [44]. It is therefore reasonable to suggest that the monotonic decrease of resonance frequencies is dominated by the effective TCE_Y of the heterostructure stack.

B. Self-Sustaining MEMS Oscillator

To enable real-time tracking of the resonance frequency, we need to build a self-sustaining oscillator and do closed-loop measurement. However, the large electrical background arising from parasitic effects and impedance mismatch makes it difficult to satisfy the Barkhausen criteria at the resonance frequency [45], particularly when the frequency strongly shifts with temperature. Fig. 7 shows the equivalent circuit model of the PZT MEMS, and the simulated resonance in Cadence. A large feedthrough capacitance (C_f) of 141pF is extracted, which may originate from the global bottom electrode for all the devices on the chip. To null the electrical background and enable higher signal-to-background ratios, we build a balanced bridge circuit with two devices operating at different frequencies but with similar electrical background on the same chip. Fig. 8a shows the bridge circuit, which primarily consists of a 180° phase shifter and an attenuator. By carefully adjusting the attenuator, the electrical background can be effectively minimized (Fig. 8b).

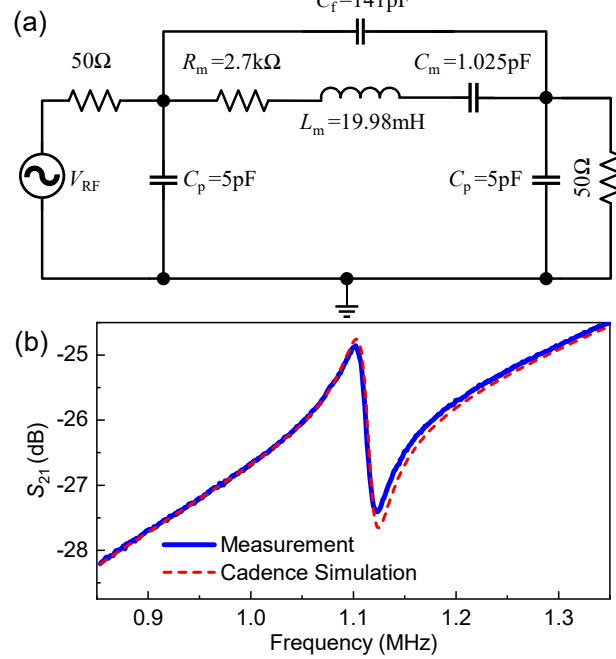


Fig. 7. Equivalent circuit model of the PZT MEMS and the simulated resonance response, which matches the measurement well.

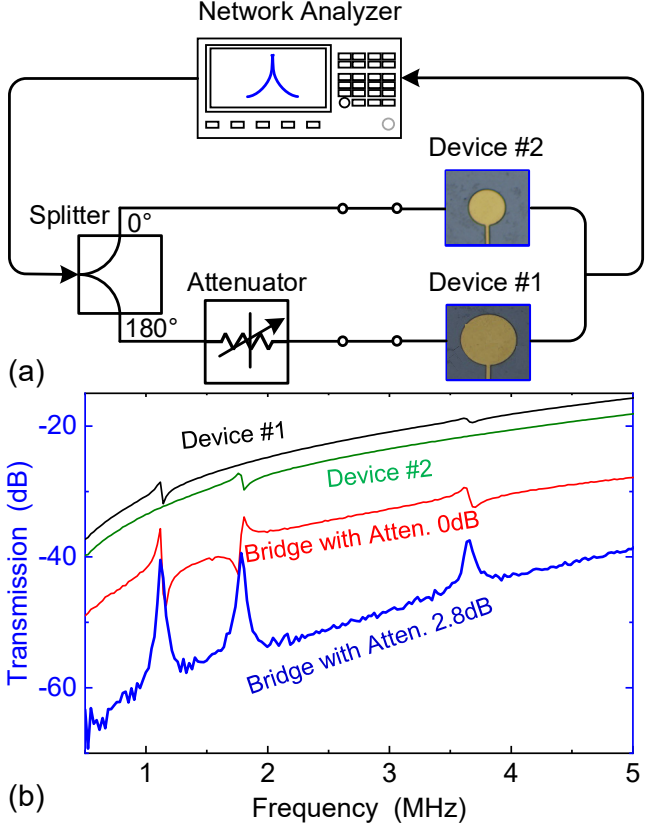


Fig. 8. (a) Balanced bridge circuit scheme. (b) Measured resonance spectra for Device #1, #2, and the balanced bridge with the attenuator set at 0dB and 2.8dB, respectively.

We then build a self-sustaining MEMS oscillator using the PZT MEMS resonator with the diagram shown in Fig. 1b. We first perform open-loop measurement to calibrate on meeting the Barkhausen criteria [45], with the overall open-loop gain slightly greater than 0dB near the resonance frequency and the overall phase shift to be $2n\pi$, where n is an integer. After satisfying the Barkhausen criteria, we close the loop and measure the stable self-oscillation both in frequency domain and time domain (Fig. 9a-b). We characterize the oscillator's performance by measuring its frequency stability. From the time-domain tracked frequency data trace, we calculate the Allan deviation [46] (Fig. 9c) from

$$\sigma_{A}(\tau_{A}) = \left[\frac{1}{2(N-1)} \sum_{i=1}^{N-1} \left(\frac{\bar{f}_{i+1} - \bar{f}_{i}}{f_{0}}\right)^{2}\right]^{1/2}, \tag{8}$$

where $\overline{f_t}$ is the measured average frequency in the i_{th} discrete time interval of τ_A . The Allan deviation data gives us the short-term frequency stability $\sigma_A \approx 2 \times 10^{-7}$ at averaging time $\tau_A < 5$ s, and long-term frequency stability $\sigma_A \approx 1 \times 10^{-6}$ at $\tau_A = 1000$ s (Fig. 9c). We then examine the phase noise behavior using the phase noise module in a spectrum analyzer. In the phase noise plot, we see two main regions. Phase noise first decreases in 100Hz to 8kHz range, largely following a $1/f^2$ power law, suggesting it is dominated by thermal noise. Phase noise flattens out beyond 10kHz offset frequency and then decreases again (Fig. 9d).

C. Closed-Loop TCf

To further explore the temperature-dependent resonance of the PZT MEMS, we have done closed-loop TCf measurement

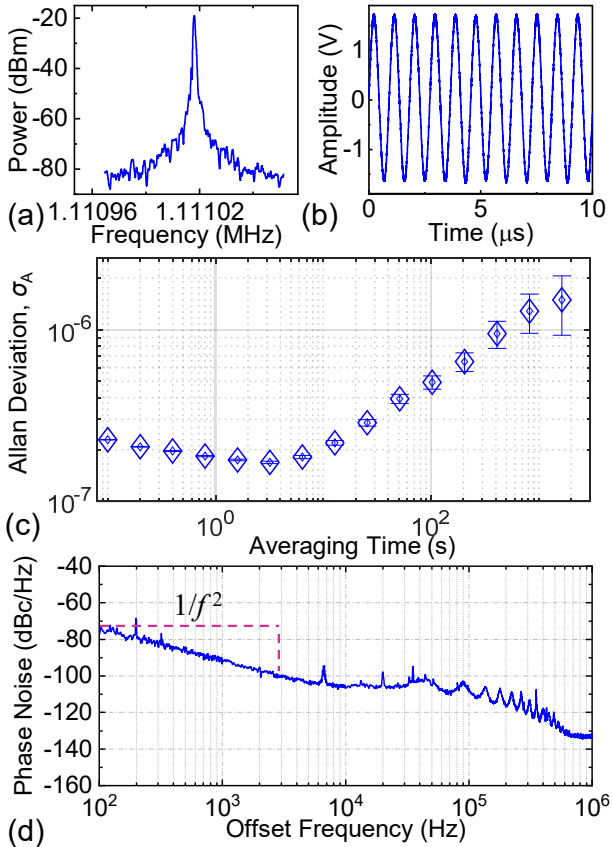


Fig. 9. Self-sustaining PZT MEMS oscillator characteristics from measurements. (a) Oscillator output spectrum. (b) Time-domain waveform. (c) Phase noise. (d) Allan deviation.

on the self-sustaining oscillator. We gradually increase the voltage applied to the ceramic heater from 0V to 9V (Fig. 10a). The resistance of the commercial resistive temperature sensor increases from 109Ω to 150Ω , corresponding to a change of temperature from 25°C to 132°C . Fig. 10b shows the frequency variation versus time. The PZT MEMS devices respond rapidly to the changes in temperature. However, it takes ~15 minutes for the frequency to be stabilized. This could be attributed to at least two factors. One effect may be caused by the slow heating process of the ceramic heater. Another may result from the slow heat transfer from the heater to the MEMS devices.

To better understand the temperature-dependent resonance of the PZT device, we conduct and compare the TCf measured in different scenarios, *i.e.*, different mounting scheme, in air or vacuum, and closed loop or open loop. To improve thermal conduction and safeguard the wires, we add a slim Cu cushion between the heater and the ceramic package. Then, raising the temperature of the heater results in a prompt response from the temperature sensor and a corresponding rapid response from the MEMS device frequency in all scenarios. This

TCF MEASURED FROM PZT MEMS DEVICES

Modality	Heater	Cushion	Pressure	Temperature [°C]	TCf ₁ [ppm/°C]
Resonator	Ceramic	No	Air	25 to 211	-193
Resonator	Ceramic	Yes	Air	25 to 132	-174
Resonator	Peltier	Yes	50mTorr	0 to 125	-125
Oscillator	Ceramic	Yes	Air	25 to 132	-88
Oscillator	Peltier	Yes	50mTorr	0 to 125	-38

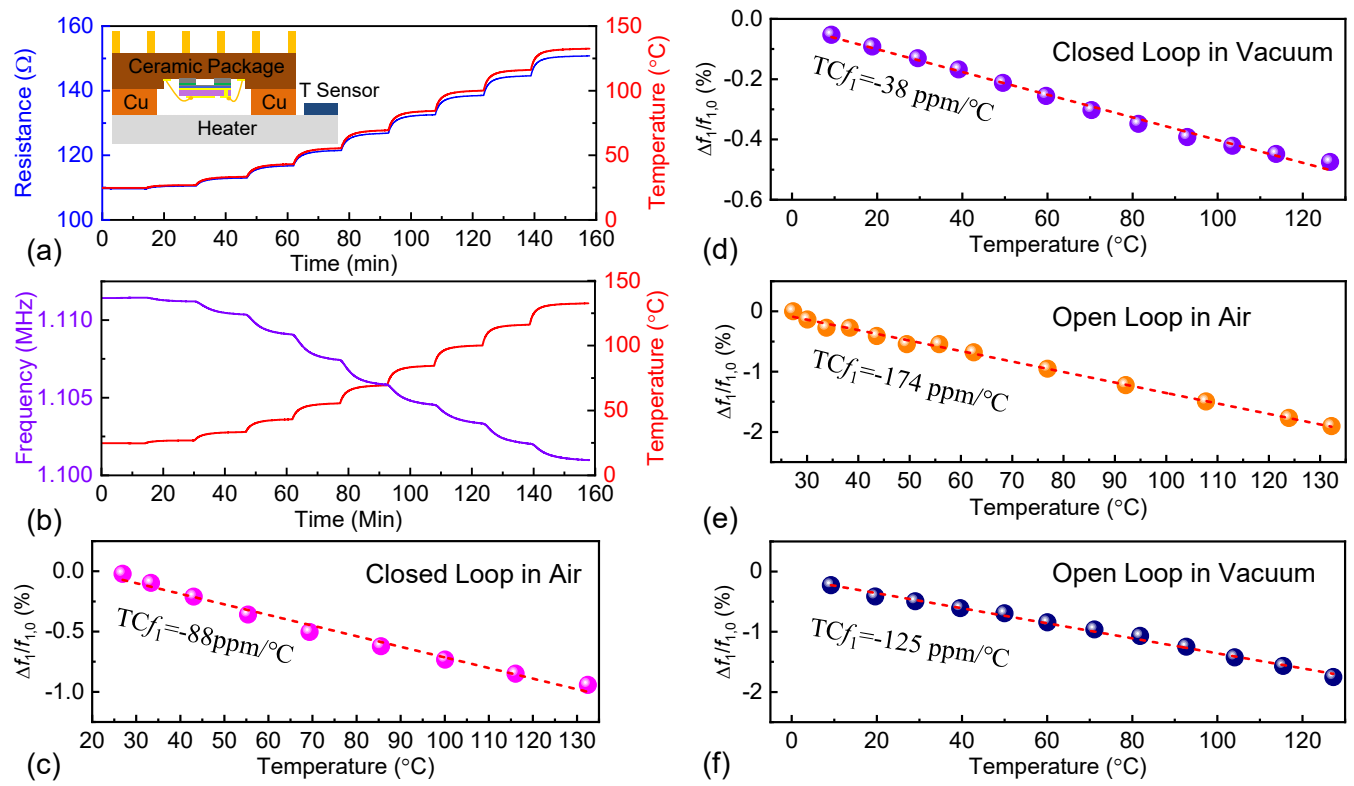


Fig. 10. TCf measured in different scenarios. (a) Resistance and temperature read from a resistive temperature sensor. The inset depicts the diagram illustrating the arrangement of the heater, temperature sensor, MEMS, and Cu cushion. (b) Real-time tracking of the frequency of the self-sustaining oscillator. (c) Fractional frequency shift $(\Delta f_1/f_{1,0})$ with varying temperature extracted from closed-loop measurement in air, where reference frequency $f_{1,0}$ is the frequency measured at room temperature. The averaged TCf is obtained by linear fitting of the $\Delta f_1/f_{1,0}$ versus temperature plot. (d) Closed-loop TCf in 50mTorr vacuum. (e) Open-loop TCf in air. (f) Open-loop TCf in 50mTorr vacuum.

simultaneous, quick response from both resistance and frequency are indicative of swift heat transfer. To extract the TCf, we take the temperature and frequency values after both are stabilized. The fractional downshift of the resonance frequency for the first mode $(\Delta f_1/f_{1,0})$ measured in different scenarios are shown in Fig. 10c-e and the extracted TCf₁ values are summarized in Table II.

The absolute open-loop TCf₁ decreases from 193ppm/°C to 174ppm/°C when the gap increases by 1mm by adding the Cu cushion, as shown in the inset of Fig. 10a, which may result from the lower heating efficiency. The absolute TCf_1 measured in air is ~50ppm/°C larger than that measured in vacuum in both open-loop and closed-loop configurations. This indicates that the heat convection has been suppressed by removing air molecules. By means of the processes of heat convection and conduction, the heater will transfer heat to the MEMS chip through the air trapped in the narrow space (totally ~2mm gap) between the heater and the chip. In a vacuum of 50mTorr, however, heat convection has been suppressed, which further lower the actual temperature of the MEMS chip than that read from the commercial temperature sensor attached directly on top of the heater ($T_{\text{MEMS in Air}} < T_{\text{Sensor}}$ and $T_{\text{MEMS in Vacuum}} < T_{\text{MEMS}}$ $_{\rm in~Air}$ < $T_{\rm Sensor}$, where $T_{\rm Sensor}$ is the temperature read from the commercial temperature sensor, see inset of Fig. 10a). This further leads to a smaller change in the resonance frequency $(\Delta f_{\text{Vacuum}} < \Delta f_{\text{Air}})$ and smaller measured TC f_1 in the case of vacuum.

Note that the absolute TCf_1 values extracted from closed loop are lower than that obtained from open loop. Such

difference in TCf₁ measured from open-loop and closed-loop configurations has also been reported in AlN solid mounted resonator [47], which can be attributed to the temperature instability of the electronics composing the oscillator. However, in our work, only the MEMS resonator is heated within the loop. The detailed mechanisms causing the difference between open-loop TCf and closed-loop TCf necessitates further investigation.

D. Dual-Mode Frequency Tracking by PLL

Multimode resonances have been exploited to resolve the position and mass of nanoparticles with high throughput and high resolution [48],[49]. The dual-mode oscillation scheme has been demonstrated as an effective method for achieving precise temperature sensing across a wide temperature range. In a particular device with the 1st and 2nd modes simultaneously excited, the resulting beat frequency (i.e., the difference between the two frequencies) can provide an accurate measure of the resonator's response to temperature changes. Because both modes are produced by the same resonator, any relative changes in their TCfs are inherently linked. As a result, any higher-order variations in one mode will be mirrored in the other, creating a near-linear function of temperature with respect to the beat frequency. For example, it is worth noting that mass loading resulting from random particle deposition on the device can cause a nonlinear decrease in the frequencies of the two modes as temperature increases. However, by relying on the beat frequency of these two modes, it is possible to effectively decouple the effects of mass loading from the resonator's temperature response.

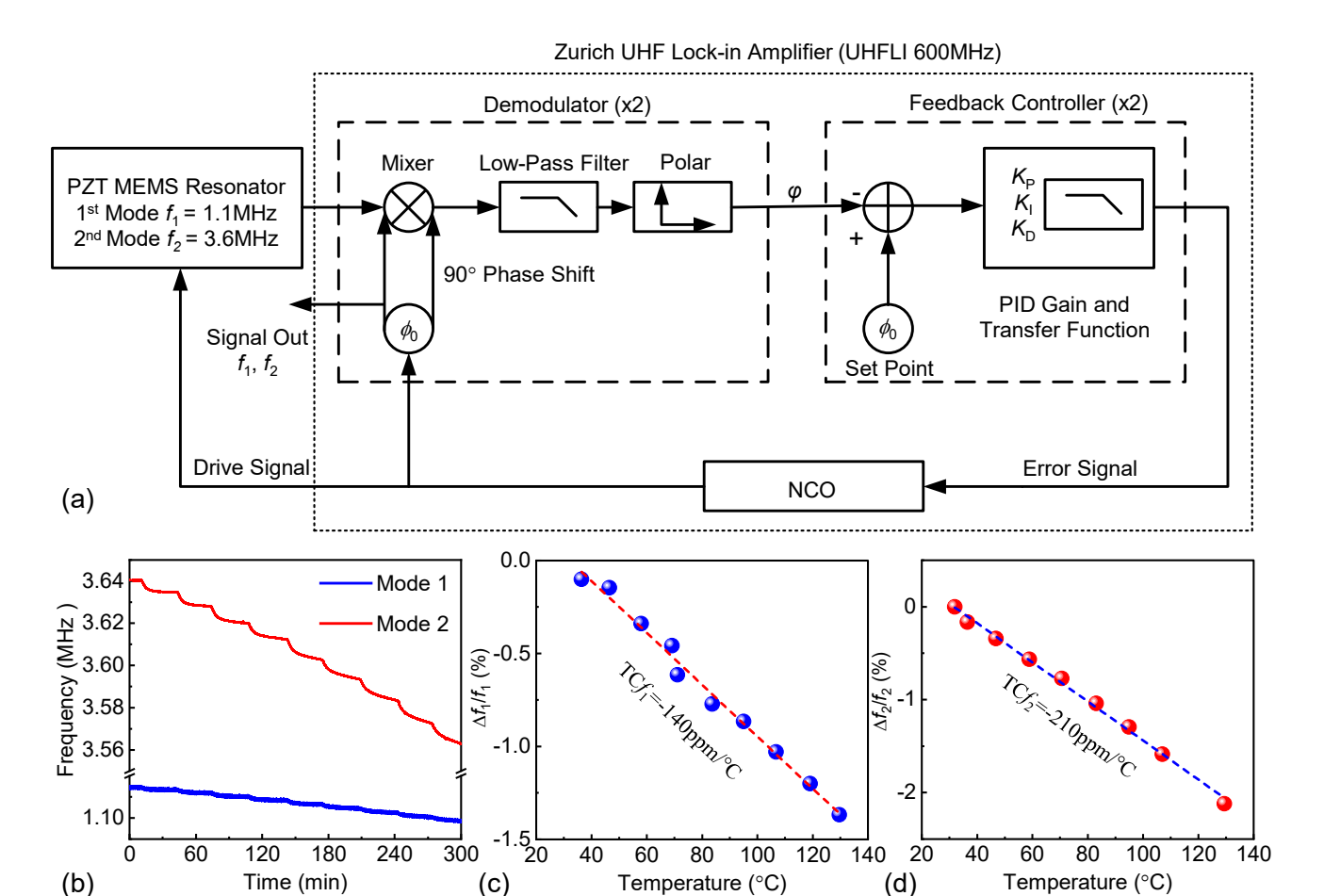


Fig. 11. Dual-mode frequency tracking by PLL. (a) PLL circuit diagram. (b) Real-time tracking of the dual-mode resonance frequency using Zurich UHFLI 600 MHz lock-in amplifier. (c) Fractional frequency shift $(\Delta f_1/f_{1,0})$ with varying temperature, where $f_{1,0}$ is the fundamental-mode resonance frequency measured at room temperature. The averaged TC f_1 is obtained by linear fitting of the $\Delta f_1/f_{1,0}$ versus temperature plot. (d) Fractional frequency shift $(\Delta f_2/f_{2,0})$ with varying temperature, where $f_{2,0}$ is the 2^{nd} mode resonance frequency measured at room temperature. The averaged TC f_2 is obtained by linear fitting of the $\Delta f_2/f_{2,0}$ versus temperature plot.

PZT MEMS resonator demonstrated in this work exhibits large absolute TCf values exceeding 200ppm/°C for the first three modes, showcasing its strong potential for on-chip temperature sensing with high resolution. To validate its feasibility, we further demonstrate the dual-mode frequency tracking by PLL in real time. In a PLL, the output of a low-noise oscillator (numerically controlled oscillator (NCO) which generates the reference signal in Fig. 11a) is locked in phase and frequency with the input signal (output from PZT MEMS in Fig. 11a) through a feedback control mechanism. It compares the phase of the input signal with that of the reference signal and then shifts the phase of the output signal (error signal in Fig. 11a) to match the input signal. PLLs are commonly used in radio frequency and microwave applications to lock local oscillators to signals from remote transmitters, and in other applications such as clock synchronization, frequency synthesis, and signal modulation. For sensing applications, PLL is used to stabilize and follow the input signal's resonance frequency. It is extensively used for tracking micro/nanomechanical vibrations [50], [51], [52], [53], [54] and for atomic force microscopy [55]. Here we employ PLL to track frequency shifts for performing the frequency stability measurements as well as for tracking real-time multimode frequency shifts caused by temperature change.

Fig. 11a demonstrates the PLL circuit diagram, which originally takes advantage of the built-in functionality of the Zurich Instruments UHFLI 600MHz lock-in amplifier. A dual phase demodulator, proportional-integral-derivative (PID) controller and an NCO are the basic building blocks of a PLL inside the UHFLI 600MHz lock-in amplifier. These form a negative feedback loop, and the mixer (phase detector) detects the phase difference between the signal from the MEMS device and the reference oscillator. The PZT MEMS under test in the Zurich instrument serves as the frequency determining element of the circuit, with PID feedback controller regulating the frequency of the NCO. The transfer function for the error signal is determined by the PID gains, which are in turn controlled by the feedback controller and the PID parameters. The transfer function begins to filter out fluctuations with a time scale that is less than the corner frequency. Based on mechanical Q, center frequency, required PLL bandwidth, locking range, and phase setpoint, the lock-in 'advisor' program automatically calculates the PID settings. The 'advisor' uses a 1st order transfer function simulation to compute a set of feedback gain parameters that it predicts to best match the specified bandwidth. This is accomplished by employing a numerically optimized technique for loop dynamics.

We employ two demodulators and two PID controllers to

perform dual-mode PLL measurement with device in 50mTorr vacuum. The dual mode (1st mode and 2nd mode) frequency shifts of the PZT device are measured simultaneously by increasing the temperature from 25°C to 132°C (Fig. 11b). The fractional frequency shifts of the two modes with varying temperature are shown Fig. 11c and Fig. 11d. We find that the 2nd mode's frequency shift is higher than the 1st mode with the same temperature change which signifies that the 2nd mode has a higher TCf compared to the 1st mode. This is also consistent with the open-loop TCf measurement shown in Fig. 6. The average TCfs of the two modes are obtained by linear fitting of the fractional frequency shifts with temperature change which yields $TCf_1=-140 \text{ ppm/}^{\circ}\text{C}$ and $TCf_2=-210 \text{ppm/}^{\circ}\text{C}$. Interestingly, the absolute TCfs of the two modes measured from PLL in 50mTorr vacuum are ~50ppm/°C lower than that obtained from open-loop measurements in air (with TCf₁=-193ppm/°C and $TCf_2=-268ppm/^{\circ}C$). As discussed before, this may be related to the suppressed heat transfer by removing air molecules trapped in the small gap between the heater and MEMS chip (see Fig. 10a inset).

V. CONCLUSION

In conclusion, we have experimentally demonstrated an integrated multimode resonant MEMS temperature sensor by exploiting a thin film ceramic PZT piezoelectric micromachined transducers in the MHz range. We have designed and fabricated the PZT MEMS transducers operating in flexural mode by using wafer bonding and CMP techniques. All the three resonance modes exhibit excellent linearity and high responsivity to temperature variations from 25°C to 211°C, with TCf ~ -200ppm/°C to -270ppm/°C for open-loop measurement. A balanced bridge circuit with two devices on the same chip is built to null the electrical background and enable higher signal-to-background ratios. We have demonstrated temperature sensing with real-time tracking of the resonance frequency using a PLL. We have built a self-sustaining PZT MEMS oscillator and measure the closed-loop TCf in different scenarios. The absolute TCf measured in air is ~50ppm/°C larger than that measured in vacuum in both open-loop and closed-loop configurations, which indicates that heat convection and conduction have been suppressed by removing air molecules.

REFERENCES

- [1] S. Fan, R. Wei, L. Zhao, X. Yang, L. Geng, P. X.-L. Feng, "An ultralow quiescent current power management system with maximum power point tracking (MPPT) for batteryless wireless sensor applications," *IEEE Trans. Power Electron.*, vol. 33, no. 9, pp. 7326–7337, Sep. 2018.
- [2] S. Fan, X.-Q. Zheng, R. Wei, J. S. Pulskamp, R. Rudy, R. G. Polcawich, P. X.-L. Feng, "mm-Scale and MEMS piezoelectric energy harvesters powering on-chip CMOS temperature sensing for IoT applications," in Proc. of the 19th Int. Solid-State Sensors, Actuat. Microsyst. Conf., (Transducers 2017), Kaohsiung, Taiwan, 2017, pp. 1848–1850.
- [3] R. Wei, A. Boggs, S. Maley, P. X.-L. Feng, "Self-powering wireless sensors for temperature sensing and monitoring in power generation applications," SPIE Proc. 10970, Sensors & Smart Structures Technologies for Civil, Mechanical, & Aerospace Systems, 109700V, Denver, CO, Mar. 2019.
- [4] H.-C. Lee and K.-H. Ke, "Monitoring of large-area IoT sensors using a LoRa wireless mesh network system: Design and evaluation," *IEEE Trans. Instrum. Meas.*, vol. 67, no. 9, pp. 2177–2187, Mar. 2018.

- [5] A. I. Sunny, A. Zhao, L. Li, and S. K. Kanteh Sakiliba, "Low-cost IoT-based sensor system: A case study on harsh environmental monitoring," *Sensors*, vol. 21, no. 1, Art. no. 214, Dec 2020.
- [6] W. Sui, X.-Q. Zheng, J.-T. Lin, J. Lee, J. L. Davidson, R. A. Reed, R. D. Schrimpf, B. W. Alphenaar, M. L. Alles, and P. X.-L. Feng, "Effects of ion-induced displacement damage on GaN/AlN MEMS resonators," *IEEE Trans. Nucl. Sci.*, vol. 69, no. 3, pp. 216–224, Jan. 2022.
- [7] J. Yang, "A harsh environment wireless pressure sensing solution utilizing high temperature electronics," *Sensors*, vol. 13, no. 3, pp. 2719–2734, Feb. 2013.
- [8] A. Ghosh, C. Zhang, S. Q. Shi, and H. Zhang, "High-temperature gas sensors for harsh environment applications: A review," *CLEAN–Soil, Air, Water*, vol. 47, no. 8, Art. no. 1800491, Aug. 2019.
- [9] X. Q. Bao, W. Burkhard, V. V. Varadan, and V. K. Varadan, "SAW temperature sensor and remote reading system," in *Proc. IEEE Int. Ultrason. Symp.*, Denver, CO, USA, 1987, pp. 583–586.
- [10] S. Ren, W. Yuan, D. Qiao, J. Deng, and X. Sun, "A micromachined pressure sensor with integrated resonator operating at atmospheric pressure," *Sensors*, vol. 13, no. 12, pp. 17006–17024, Dec. 2013.
- [11] T. Ueda, F. Kohsaka, T. Iino, and D. Yamazaki, "Temperature sensor using quartz tuning fork resonator," in *Proc.* 40th Annu. Symp. on Freq. Control, Philadelphia, Pennsylvania, USA, 1986, pp. 224–229.
- [12] H. Fatemi, M. J. Modarres-Zadeh, and R. Abdolvand, "Passive wireless temperature sensing with piezoelectric MEMS resonators," in *Proc. IEEE 28th Int. Conf. Micro Electro Mech. Syst. (MEMS)*, Estoril, Portugal, 2015, pp. 909–912.
- [13] P. Song, Z. Ma, J. Ma, L. Yang, J. Wei, Y. Zhao, M. Zhang, F. Yang, and X. Wang, "Recent progress of miniature MEMS pressure sensors," *Micromachines*, vol. 11, no. 1, Art. no. 56, Jan. 2020.
- [14] K. Park, N. Kim, D. T. Morisette, N. R. Aluru, and R. Bashir, "Resonant MEMS mass sensors for measurement of microdroplet evaporation," *J. Microelectromechanical Syst.*, vol. 21, no. 3, pp. 702–711, Jun. 2012.
- [15] J. Xu, M. Bertke, H. S. Wasisto, and E. Peiner, "Piezoresistive microcantilevers for humidity sensing," *J. Micromech. Microeng.*, vol. 29, no. 5, Art. no. 053003, Apr. 2019.
- [16] W. Sui, H. Wang, J. Lee, A. Qamar, M. Rais-Zadeh, and P. X.-L. Feng, "AlScN-on-SiC thin film micromachined resonant transducers operating in high-temperature environment up to 600°C," *Adv. Funct. Mater.*, vol. 32, no. 34, Art. no. 2202204, Aug. 2022.
- [17] A. Qamar, S. R. Eisner, D. G. Senesky, and M. Rais-Zadeh, "Ultra-high-Q gallium nitride SAW resonators for applications with extreme temperature swings," J. Microelectromechanical Syst., vol. 29, no. 5, pp. 900–905, Jun. 2020.
- [18] W. Sui, X.-Q. Zheng, J.-T. Lin, B. W. Alphenaar, and P. X.-L. Feng, "Thermal response and TCf of GaN/AlN heterostructure multimode micro string resonators from -10°C up to 325°C," J. Microelectromechanical Syst., vol. 30, no. 4, pp. 521–529, Jun. 2021.
- [19] J. Streque, J. Camus, T. Laroche, S. Hage-Ali, H. M'Jahed, M. Rammal, T. Aubert, M. A. Djouadi, S. Ballandras, and O. Elmazria, "Design and characterization of high-Q SAW resonators based on the AlN/Sapphire structure intended for high-temperature wireless sensor applications," *IEEE Sens. J.*, vol. 20, no. 13, pp. 6985–6991, Mar. 2020.
- [20] J. Yang, B. Hamelin, and F. Ayazi, "Investigating elastic anisotropy of 4H-SiC using ultra-high Q bulk acoustic wave resonators," J. Microelectromechanical Syst., vol. 29, no. 6, pp. 1473–1482, Sep. 2020.
- [21] Q. Xie, N. Wang, C. Sun, A. B. Randles, P. Singh, X. Zhang, and Y. Gu, "Effectiveness of oxide trench array as a passive temperature compensation structure in AlN-on-silicon micromechanical resonators," *Appl. Phys. Lett.*, vol. 110, no. 8, Art. no. 083501, Feb. 2017.
- [22] M. Reusch, K. Holc, V. Lebedev, N. Kurz, A. Zukauskaite, and O. Ambacher, "Temperature cross-sensitivity of AlN-based flexural plate wave sensors," *IEEE Sens. J*, vol. 18, no. 19, pp. 7810–7818, Jul. 2018.
- [23] S. Fei and H. Ren, "Temperature characteristics of a contour mode MEMS AlN piezoelectric ring resonator on SOI substrate," *Micromachines*, vol. 12, no. 2, Art. no. 143, Jul. 2021.
- [24] A. K. Samarao and F. Ayazi, "Temperature compensation of silicon micromechanical resonators via degenerate doping," in *IEDM Tech. Dig.*, Baltimore, MD, USA, 2009, pp. 1–4.
- [25] A. Hajjam, A. Logan, and S. Pourkamali, "Doping-induced temperature compensation of thermally actuated high-frequency silicon micromechanical resonators," J. Microelectromechanical Syst., vol. 21, no. 3, pp. 681–687, Feb. 2012.

- [26] M. Moosavifar, A. Ansari, and M. Rais-Zadeh, "An AlN-on-Si resonant IR sensor array with a large temperature coefficient of frequency," in *Proc. IEEE Sensors*, Orlando, FL, USA, 2016, pp. 1–3.
- [27] W. Sui, X.-Q. Zheng, J.-T. Lin, B. W. Alphenaar, and P. X.-L. Feng, "Temperature dependence of multimode gallium nitride/aluminum nitride (GaN/AlN) heterostructure string resonator," in *Proc. IEEE Int. Conf. Micro Electro Mech. Syst. (MEMS)*, Gainesville, FL, USA, 2021, pp. 478–481.
- [28] A. C. Fischer, F. Forsberg, M. Lapisa, S. J. Bleiker, G. Stemme, N. Roxhed, and F. Niklaus, "Integrating MEMS and ICs," *Microsyst. Nanoeng.*, vol. 1, no. 1, pp.1–16, May 2015.
- [29] C. G. Hindrichsen, R. Lou-M
 øller, K. Hansen, and E. V. Thomsen, "Advantages of PZT thick film for MEMS sensors," Sens. Actuators A, Phys., vol. 163, no. 1, pp. 9–14, Jun. 2010.
- [30] G. L. Smith, J. S. Pulskamp, L. M. Sanchez, D. M. Potrepka, R. M. Proie, T. G. Ivanov, R. Q. Rudy, W. D. Nothwang, S. S. Bedair, C. D. Meyer, and R. G. Polcawich, "PZT-based piezoelectric MEMS technology," *J. Am. Ceram. Soc.*, vol. 95, no. 6, pp. 1777–1792, Apr. 2012.
- [31] M. D. Nguyen, H. N. Vu, D. H. Blank, and G. Rijnders, "Epitaxial Pb(Zr, Ti)O₃ thin films for a MEMS application," *Adv. Nat. Sci.*, vol. 2, no. 1, Art. no. 015005, Mar. 2011.
- [32] H. Wang, P. X.-L. Feng, and H. Xie, "A high-density and dual-frequency PMUT array based on thin ceramic PZT for endoscopic photoacoustic imaging," in *Proc. IEEE Int. Conf. Micro Electro Mech.* Syst. (MEMS), Gainesville, FL, USA, 2021, pp. 891–894.
- [33] H. Wang, H. Yang, H. Jiang, Z. Chen, P. X.-L. Feng, and H. Xie, "A multi-frequency pMUT array based on ceramic PZT for endoscopic photoacoustic imaging," in *Proc. of the 21st Int. Solid-State Sensors, Actuat. Microsyst. Conf.*, (Transducers 2021), Orlando, FL, USA, 2021, pp. 30–33.
- [34] A. Dangi, S. Agrawal, S. Tiwari, S. Jadhav, C. Cheng, S. Trolier-McKinstry, R. Pratap, and S.-R. Kothapalli, "Evaluation of high frequency piezoelectric micromachined ultrasound transducers for photoacoustic imaging," in *Proc. IEEE Sensors*, New Delhi, India, Oct. 2018, pp. 1–4.
- [35] W. Liao, W. Liu, J. E. Rogers, F. Usmani, Y. Tang, B. Wang, H. Jiang, and H. Xie, "Piezoelectric micromachined ultrasound transducer array for photoacoustic imaging," in *Proc. of the 17th Int. Solid-State Sensors, Actuat. Microsyst. Conf.*, (Transducers 2021), Barcelona, Spain, 2013, pp. 1831–1834.
- [36] E. E. Aktakka, R. L. Peterson, and K. Najafi, "Wafer-level integration of high-quality bulk piezoelectric ceramics on silicon," *IEEE Trans. Electron Devices*, vol. 60, no. 6, pp. 2022–2030, Jun. 2013.
- [37] C. G. Hindrichsen, R. Lou-Müller, K. Hansen, and E. V. Thomsen, "Advantages of PZT thick film for MEMS sensors," Sens. Actuators A, Phys., vol. 163, no. 1, pp. 9–14, Sep. 2010.
- [38] H. Suzuki, N. Yamaguchi, and H. Izumi, "Theoretical and experimental studies on the resonance frequencies of a stretched circular plate: Application to Japanese drum diaphragms," *Acoust. Sci. Technol.*, vol. 30, no. 5, pp. 348–354, Sep. 2009.
- [39] W. Sui, T. Kaisar, H. Wang, Y. Wu, J. Lee, H. Xie, and P. X.-L. Feng, "Thin film PZT multimode resonant MEMS temperature sensor," in Proc. IEEE Sensors, Dallas, TX, USA, 2022, pp. 1–4.
- [40] H. Wang, M. Godara, Z. Chen, and H. Xie, 2019. "A one-step residue-free wet etching process of ceramic PZT for piezoelectric transducers," Sens. Actuator A Phys., vol. 290, pp.130–136, May 2019.
- [41] U. Köbler, "The importance of the Debye bosons (sound waves) for the lattice dynamics of solids," *Int. J. Thermodyn.*, vol. 23, no. 2, pp. 59–79, May 2020.
- [42] H. Watanabe, N. Yamada, and M. Okaji, "Linear thermal expansion coefficient of silicon from 293 to 1000K," *Int. J. Thermophys.*, vol. 25, no. 1, pp.221–236, Jan. 2004.
- [43] C. Birleanu, M. Pustan, V. Merie, R. Müller, R. Voicu, A. Baracu, and S. Craciun, "Temperature effect on the mechanical properties of gold nano films with different thickness,". In *IOP Conf. Ser.: Mater. Sci. Eng.*, vol. 147, no. 1, Art. no. 012021, Aug. 2016.
- [44] J. Vanhellemont, A. K. Swarnakar, and O. Van der Biest, "Temperature dependent Young's modulus of Si and Ge," ECS Trans., vol. 64, no. 11, pp. 283–292, Aug. 2014.
- [45] X. L. Feng, C. J. White, A. Hajimiri, and M. L. Roukes, "A self-sustaining ultrahigh-frequency nanoelectromechanical oscillator," *Nat Nanotechnol*, vol. 3, no. 6, pp. 342–346, May 2008.

- [46] D. W. Allan, "Time and frequency (time-domain) characterization, estimation, and prediction of precision clocks and oscillators," *IEEE Trans. Ultrason. Ferroelectr. Freq. Control*, vol. 34, no. 6, pp. 647–654, Nov. 1987.
- [47] M. Rinaldi, A. Tazzoli, J. Segovia-Fernandez, V. Felmetsger, and G. Piazza, "High power and low temperature coefficient of frequency oscillator based on a fully anchored and oxide compensated AlN contour-mode MEMS resonator," in *Proc. IEEE Int. Conf. Micro Electro Mech. Syst. (MEMS)*, Paris, France, 2012, pp. 696–699.
- [48] M. S. Hanay, S. I. Kelber, C. D. O'Connell, P. Mulvaney, J. E. Sader, and M. L. Roukes, "Inertial imaging with nanomechanical systems," *Nat. Nanotechnol.*, vol. 10, no. 4, pp.339–344, Apr. 2015.
- [49] S. Olcum, N. Cermak, S. C.Wasserman, and S. R. Manalis, 2015. "High-speed multiple-mode mass-sensing resolves dynamic nanoscale mass distributions," *Nat. Commun.*, vol. 6, no. 1, Art. no. 7070, May 2015.
- [50] Y. T. Yang, C. Callegari, X. L. Feng, K. L. Ekinci, and M. L. Roukes, "Zeptogram-scale nanomechanical mass sensing," *Nano Lett.*, vol. 6, no. 4, pp. 583–586, Apr. 2006.
- [51] S. Olcum, N. Cermak, S. C. Wasserman, and S. R. Manalis, "High speed multiple-mode mass sensing resolves nanoscale mass distributions," *Nat. Commun.*, vol. 6, no. 7070, May 2015.
- [52] M. S. Hanay, S. Kelber, A. K. Naik, D. Chi, S. Hentz, E. C. Bullard, E. Colinet, L. Duraffourg, and M. L. Roukes, "Single-protein nanomechanical mass spectrometry in real time," *Nat. Nanotechnol.*, vol. 7, no. 9, pp. 602–608, Sep. 2012.
- [53] M. Li, H. X. Tang, and M. L. Roukes, "Ultra-sensitive NEMS-based cantilevers for sensing, scanned probe and very high frequency applications," *Nat. Nanotechnol.*, vol. 2, pp. 114–120, Feb. 2007.
- [54] L. C. Ortiz, H. K. Kwon, J. Rodriguez, Y. Chen, G. D. Vukasin, D. B. Heinz, D. D. Shin, and T. W. Kenny, "Low-power dual mode MEMS resonators with PPB stability over temperature," *J. Microelectromech. Syst.*, vol. 29, no. 2, pp. 190–201, Apr. 2020.
- [55] F. J. Giessibl, "Advances in atomic force microscopy," Rev. Mod. Phys., vol. 75, no. 749, July 2003.



Wen Sui (Graduate Student Member, IEEE) received the B.S. and M.S. degrees in mechanical engineering from Northeastern University, Shenyang, China, in 2016 and 2019, respectively. He is currently pursuing the Ph.D. degree with the Department of Electrical and Computer Engineering, University of Florida, Gainesville, USA. His major research area is wide-bandgap semiconductor MEMS/NEMS for harsh environment applications, such as gallium

nitride (GaN), aluminum scandium nitride (AlScN), and silicon carbide (SiC) MEMS for applications in high-temperature and radiative environment. He was a recipient of the Margaret A. Ross Fellowship from ECE, University of Florida, and a recipient of the Finish Line Award from Graduate School, University of Florida.



Tahmid Kaisar (Graduate Student Member, IEEE) received his B.S. degree in electrical and electronic engineering from Bangladesh University of Engineering and Technology (BUET), Dhaka, Bangladesh in 2018. He is currently pursuing the Ph.D. degree with the Department of Electrical and Computer Engineering (ECE), University of Florida, Gainesville, FL, USA. His research interests CMOS-MEMS include oscillator-based computing, MEMS/NEMS oscillator for real time

sensing and timing applications, and nonlinear dynamics of 2D material NEMS based devices. He was a recipient of the Best Research Work award at the AVS 2021 International Symposium.



Haoran Wang received the B.S. degree in measuring and control technology instruments from Tianjin University, Tianjin, China, in 2017, and the Ph.D. degree in electrical and computer engineering from the University of Florida, Gainesville, USA, in 2021. His research interests include microelectromechanical systems (MEMS), optical MEMS, micro/nano fabrication, and piezoelectric transducers. He is currently a senior scientist at Applied Materials

Inc., Sunnyvale, CA, USA.



computing.

Yihao Wu (Graduate·Student·Member, IEEE) received his B.S. degree in electronics science and technology from Beijing University of Technology (BJUT), Beijing, China in 2021. He is currently pursuing the M.S. degree with the Department of Electrical and Computer Engineering (ECE), University of Florida, Gainesville, FL, USA. His research interests include high-speed low power data converter design, such as analog to digital converter, time to digital converter, and CMOS oscillator-based quantum-inspired

> Jaesung Lee (Member, IEEE) received his Ph.D. in Electrical Engineering from Case Western Reserve University (CWRU) in 2017. Earlier, he received B.S. and M.S. degrees in Electrical Engineering from the University of Electro-Communications (UEC), Tokyo, Japan. He is currently an Assistant Professor in the Department of Electrical and Computer Engineering at the University of Texas at El Paso. His research interests have focused upon

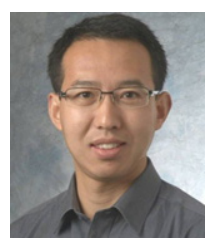


developing functional nanodevices (e.g., NEMS/MEMS, optoelectronic, phononic devices) using advanced materials (e.g., 2D crystals and wide-bandgap semiconductors), towards building integrated systems for signal processing and sensing, in both classical and quantum regimes. He is a Co-Technical Program Chair for the MEMS/NEMS Technical Group at the 69th American Vacuum Society (AVS) International Symposium & Exhibition.



Huikai Xie (Fellow, IEEE) received the B.S. degree in microelectronics from Beijing Institute of Technology, the M.S. degree in photonics from Tufts University, and the Ph.D. degree in electrical and computer engineering from Carnegie Mellon University. He worked with the University of Florida as an Assistant Professor (2002-2007), an Associate Professor with tenure (2007–2011), and a Full Professor (2011–2020). He is currently a Professor with the School of

Information and Electronics, Beijing Institute of Technology, Beijing, China. He has published over 300 technical papers, 11 book chapters, and holds over 30 US patents. His current research interests include MEMS/NEMS, optical beam steering, optical communications, LiDAR, NIR spectroscopy, and optical microendoscopy. He is a fellow of SPIE. He is also an Associate Editor of the IEEE SENSORS LETTERS and Sensors and Actuators A: Physical.



Philip X.-L. Feng (Senior Member, IEEE) received his Ph.D. degree in Electrical Engineering (EE) from the California Institute of Technology (Caltech), Pasadena, CA, in 2007. He is currently a Professor in the Department of Electrical and Computer University Engineering, of Gainesville, Florida, USA. His research is primarily focused on emerging solid-state devices and systems,

nano/microelectromechanical systems (NEMS/MEMS), atomic laver semiconductors and 2D devices, silicon carbide (SiC) and other advanced semiconductors, quantum devices based on SiC and 2D materials, as well as their integration with state-of-the-art ICs and optical/photonic technologies. He is an alumnus of the National Academy of Engineering (NAE) U.S. Frontier of Engineering (USFOE) program and subsequently a recipient of the NAE Grainger Foundation Frontiers of Engineering (FOE) Award. His awards also include the Presidential Early Career Award for Scientists and Engineers (PECASE) and the National Science Foundation CAREER Award. He and his students have won six Best Paper/Presentation Awards at IEEE and other international conferences. He has mentored/co-mentored 13 Ph.D. students to successful dissertation defense, mentored 8 postdoctoral scholars, and also supervised 15 M.S. students with theses or research projects. He has served on the Technical Program Committees (TPCs) for the IEEE International Electron Devices Meeting (IEDM), the IEEE International Conference on Micro Electro Mechanical Systems (MEMS), International Conference on Solid-State Sensors, Actuators and Microsystems (Transducers), the IEEE International Frequency Control Symposium (IFCS) & European Frequency and Time Forum (EFTF), IEEE SENSORS, IEEE NANO, and other international conferences and workshops. He served as a Track Chair for IEEE SENSORS 2016-2017, and as the TPC Group 4 Chair for the IEEE IFCS 2018, IFCS-EFTF 2019, and IFCS-ISAF 2020. He has also served as the Technical Program Chair for the MEMS/NEMS Technical Group at the 61st to 63rd American Vacuum Society (AVS) International Symposium & Exhibition. He is also a co-organizer and the technical chair of the SiC Materials & Devices Workshop (since 2017). He has served as a Chair for the 34th IEEE International Conference on Micro Electro Mechanical Systems (IEEE MEMS 2021).